HHS Public Access

Author manuscript

Opt Lett. Author manuscript; available in PMC 2022 December 30.

Published in final edited form as:

Opt Lett. 2021 October 01; 46(19): 5059–5062. doi:10.1364/OL.436334.

Depth resolution in multifocus laser speckle contrast imaging

Shuqi Zheng[1,*], **Sheng Xiao**[2], **Lisa Kretsge**[3], **Alberto Cruz-Martín**[3], **Jerome Mertz**[2]

[1]Boston University, Department of Electrical and Computer Engineering, 8 St. Mary's St., Boston, MA 02215, USA

[2]Boston University, Department of Biomedical Engineering, 44 Cummington Mall, Boston, MA 02215, USA

[3]Boston University, Department of Biology, 5 Cummington Mall, Boston, MA 02215, USA

Abstract

Laser speckle contrast imaging (LSCI) can be used to evaluate blood flow based on spatial or temporal speckle statistics, but its accuracy is undermined by out-of-focus image blur. In this letter, we show how the fraction of dynamic versus static light scattering is dependent on focus, and describe a deconvolution strategy to correct for out-of-focus blur. With the aid of a z-splitter which enables instantaneous multifocus imaging, we demonstrate depth-resolved LSCI that can robustly extract multi-plane structural and flow-speed information simultaneously. This method is applied to in-vivo imaging of blood vessels in a mouse cortex and provides improved estimates of blood flow speed throughout a depth range of 300 μm.

Laser speckle contrast imaging (LSCI) is a simple technique to monitor vascular structure and blood flow dynamics [1]. When laser light is sent into tissue, it becomes scattered and produces speckle patterns that are imaged by a camera. Motion of scatterers within the tissue is then revealed by changes in the speckle contrast K, either spatial [2] or temporal [3]. However, the exact relationship between scatterer motion and speckle contrast is complicated. In most cases, the problem is simplified by phenomenologically separating the speckle dynamics into two time scales, one fast relative to the camera exposure time and the other so slow that it can be considered static [4, 5]. With this simplification, the time constant τ_c associated with the fast (or dynamic) speckle component is then related to motion within the sample by way of a theoretical model [6].

Critical to the assessment of τ_c is an accurate determination of the relative weighting between dynamic and static speckle components. In practice, this can be achieved with multi [6, 7] and single exposure [8, 9] LSCI, after correcting for spatial integration [10, 11] and detection noise [6, 12]. However, the weighting between dynamic and static components also depends on imaging focus. Efforts to address this focus problem have included extended depth of field (EDOF) LSCI with wavefront coding [13], misfocus-measurement and correction using kurtosis analysis [14], and multifocus image fusion [15]. For example,

[*]Corresponding author: sqzheng@bu.edu.

Disclosures. The authors declare no conflicts of interest.

in reference [13], image deconvolution was applied to the contrast map to enhance the fidelity of flow index ($1/K^2$) reconstruction, though without considering the possibility of static scattering.

In this letter, we examine the effect of image focus on LSCI. In particular, we examine its effect on the relative weighting of dynamic versus static speckle components, and show that this weighting suffers from blurring in a manner similar to incoherent fluorescence imaging. This blurring can be corrected for by deconvolution, as we verify by simulations and experiment, thus enabling the recovery of depth resolution. To facilitate our study, we make use of a device called a z-splitter prism [16], which provides instantaneous multifocus imaging with a single camera and no moving parts. Finally, we demonstrate the application of our approach to in-vivo brain imaging in a mouse. Our approach is best demonstrated with medium-sized blood vessels 10–100 μm in diameter, since these are well-defined structures that can be well resolved, causing the effects of defocus to be most apparent.

We start by writing the instantaneous light field at the object plane as a sum of a dynamic field $E_{0d}(\boldsymbol{\rho}, t)$ and a static field $E_{0s}(\boldsymbol{\rho})$:

$$E_0(\boldsymbol{\rho}, t) = E_{0d}(\boldsymbol{\rho}, t) + E_{0s}(\boldsymbol{\rho}) \tag{1}$$

where $\boldsymbol{\rho}$ is the transverse spatial coordinate. The dynamic component fraction at the object plane is defined by

$$\xi_0(\boldsymbol{\rho}) = \frac{\langle I_{0d}(\boldsymbol{\rho}, t)\rangle}{\langle I_{0d}(\boldsymbol{\rho}, t)\rangle + \langle I_{0s}(\boldsymbol{\rho})\rangle} \tag{2}$$

where $\langle I_{0d}\rangle = \langle |E_{0d}|^2\rangle$, $\langle I_{0s}\rangle = \langle |E_{0s}|^2\rangle$ are time-averaged intensities. Note that in the literature this dynamic fraction is sometimes denoted by the symbol ρ, which has a different meaning here.

In most experimental cases, the average intensity at the object plane is highly uniform regardless of whether the sample is dynamic or static. In other words, it is difficult to distinguish dynamic from static sample components based on average intensity alone. We can directly incorporate this intensity homogeneity into Eq.(1) by writing

$$E_0(\boldsymbol{\rho}, t) = \sqrt{\xi_0(\boldsymbol{\rho})} S_d(\boldsymbol{\rho}, t) + \sqrt{1 - \xi_0(\boldsymbol{\rho})} S_s(\boldsymbol{\rho}) \tag{3}$$

where $S_d(\boldsymbol{\rho}, t)$ and $S_s(\boldsymbol{\rho})$ are underlying dynamic and static speckle fields in the sample, each of average intensity of $\bar{I}_0 = \langle I_{0s}(\boldsymbol{\rho})\rangle + \langle I_{0d}(\boldsymbol{\rho}, t)\rangle$. We thus find $\left\langle |E_0(\boldsymbol{\rho}, t)|^2 \right\rangle = \bar{I}_0$ independent of $\xi_0(\boldsymbol{\rho})$.

Next we consider a coherent imaging system of amplitude point spread function H. The field at the image (camera) plane is [17]

$$E(\boldsymbol{\rho}, t) = \int H(\boldsymbol{\rho} - \boldsymbol{\rho}', z) E_0(\boldsymbol{\rho}', t) d^2\boldsymbol{\rho}' := E_d(\boldsymbol{\rho}, t) + E_s(\boldsymbol{\rho}) \tag{4}$$

where z corresponds to defocus and

$$E_d(\boldsymbol{\rho},t)=\int H(\boldsymbol{\rho}-\boldsymbol{\rho}',z)\sqrt{\xi_0(\boldsymbol{\rho}')}S_d(\boldsymbol{\rho}',t)d^2\boldsymbol{\rho}' \tag{5}$$

$$E_s(\boldsymbol{\rho})=\int H(\boldsymbol{\rho}-\boldsymbol{\rho}',z)\sqrt{1-\xi_0(\boldsymbol{\rho}')}S_s(\boldsymbol{\rho}')d^2\boldsymbol{\rho}'. \tag{6}$$

With the assumption that the underlying speckle fields arise from multiple scattering in the sample from all directions, then both S_s and S_d can be regarded as effectively δ-correlated in space when compared to the imaging resolution.

The averaged intensities of the dynamic and static speckle components become then

$$\langle I_d(\boldsymbol{\rho},t)\rangle=\bar{I}_0\int PSF(\boldsymbol{\rho}-\boldsymbol{\rho}',z)\xi_0(\boldsymbol{\rho}')d^2\boldsymbol{\rho}' \tag{7}$$

$$\langle I_s(\boldsymbol{\rho})\rangle=\bar{I}_0\int PSF(\boldsymbol{\rho}-\boldsymbol{\rho}',z)[1-\xi_0(\boldsymbol{\rho}')]d^2\boldsymbol{\rho}' \tag{8}$$

where $PSF=|H|^2$ is the incoherent point spread function.

Therefore the measured dynamic fraction $\xi(\boldsymbol{\rho})$ at image plane can be shown to be

$$\xi(\boldsymbol{\rho})=\frac{\langle I_d(\boldsymbol{\rho},t)\rangle}{\langle I_s(\boldsymbol{\rho})\rangle+\langle I_d(\boldsymbol{\rho},t)\rangle}=\int PSF(\boldsymbol{\rho}-\boldsymbol{\rho}',z)\xi_0(\boldsymbol{\rho}')d^2\boldsymbol{\rho}' \tag{9}$$

Equation (9) shows that ξ and ξ_0 are related by a convolution with the incoherent PSF. As a result the measured $\xi(\boldsymbol{\rho})$, which is implicitly dependent on z, can be subject to defocus induced error, while $\xi_0(\boldsymbol{\rho})$, which represents the actual spatial distribution of the dynamic scatterers within the sample, is free from such error. As will be shown below, the latter can be retrieved from the former by deconvolution.

To obtain our data, we performed standard LSCI with a 6-plane z-splitter [16] [Fig. 1(a)]. This enabled us to simultaneously image six planes within the sample, separated by distances $\Delta z = L/M^2n$, where L is the length of each constituent prism, n is the refractive index of the prism glass, and M is the lateral magnification at the intermediate image plane after tube lens $L1$. In our case, we used a 10×/0.3NA objective lens (Olympus PLN) with $L1$ = 200 mm, leading to Δz = 66 μm. The intermediate image at the prism exit was re-imaged onto the camera (ORX-10G-71S7, Teledyne Flir) through a relay lens pair ($L2/L3$ = 200/75) to match the sensor size. A crossed polarizer P was placed in the detection path to reduce surface scattering. A HeNe laser beam (17 mW, N-LHP-925, Newport) was expanded and directed onto the sample with a spot size of roughly 2 mm.

Figure 1(b) illustrates the processing procedure. For each imaging event, N frames are sequentially acquired at a 75 Hz frame rate. The contrast is evaluated from the speckle intensity as

$$K = \frac{\sigma(I)}{\langle I \rangle} \tag{10}$$

where $\sigma(\cdot)$ is the standard deviation and $\langle \cdot \rangle$ corresponds to a spatial or temporal average. The spatial contrast K_s is calculated in a sliding window $N_s \times N_s$ pixels in size and averaged over N frames. The temporal contrast K_t is calculated at each pixel over N_t consecutive frames and then averaged in the local spatial window. Corrections are made for dark noise and shot noise with pre-calibrated camera gain and dark-noise variance as described in [12]. The fraction of dynamically scattered light is then determined from the noise-corrected speckle contrast by [8]

$$\xi = 1 - \sqrt{\frac{K_s^2 - K_t^2}{\beta}} \tag{11}$$

where β is the integration factor pre-calibrated from the local spatial contrast of a reflectance standard. In our case $\beta = 0.145$ is relatively small because of the reduced the number of camera pixels available per focal plane after introducing the z-splitter.

Once β and ξ are determined, the dynamic correlation time τ_c can be evaluated from a fit to a theoretical model. Different models have been proposed depending on the scattering regimes and particle motion types [18, 19]. As an example, we use the simplest model associated with a Lorentzian distribution of scatterer velocities which best describes the dynamics in medium-sized vessels[18], obtaining after noise correction [6, 8]

$$K_t^2(T, \tau_c) = \beta\xi^2 \frac{e^{-2x} - 1 + 2x}{2x^2} + 4\beta\xi(1-\xi)\frac{e^{-x} - 1 + x}{x^2} \tag{12}$$

where $x = T/\tau_c$ and T is the camera exposure time. We emphasize that with our z-splitter system, we can simultaneously perform these fits in all six planes. However, because of the defocus effect on ξ which causes the dynamic signal to appear less dynamic when it is out of focus, the error in these fits is minimized only for those planes where ξ is most in focus, as determined by deconvolution. In this manner, by resolving ξ in depth, we are able to synthesize a minimum-error map of τ_c that is all in focus.

To verify this, we first confirmed that ξ is imaged incoherently according to Eq. (9) by comparing LSCI with fluorescence imaging. A solution of diluted milk and rhodamine (1g/liter) was pumped through a 100 μm capillary (Polymicro, Molex) embedded in a substrate made of polydimethyl siloxane (PDMS) and titanium dioxide powder (1mg of TiO_2 per gram of PDMS). The capillary was about 80 μm below the surface. A thick slab made from the same medium was placed under the sample to increase the LSCI signal strength. Speckle and fluorescence imaging were performed sequentially by switching between laser and green LED illumination. The flow speed was controlled by a syringe pump (New Era Pump Systems, Inc). The exposure time was $T = 3$ ms. For speckle imaging, $N = 20$ frames were recorded at different defocus values as the sample was translated axially. Contrast images were then calculated with $N_s = 5$, $N_t = 20$.

In addition, we performed a numerical simulation of our experiment. Speckle fields at the object plane were computationally propagated through a simulated imaging system with the same specifications (NA, magnification) as our experimental system. Time integrated speckle patterns were produced at the image plane by averaging 10 realizations each. 20 integrated speckle images were then processed to calculate ξ. In this manner, ξ stacks obtained by both experiment and simulation could be directly compared with the fluorescence stack obtained by experiment.

Figure 2 illustrates this comparison, where the sample was axially translated a depth range of 1400 μm in steps of 25 μm. Figure 2(a–c) shows the x-z cross-sections of the resulting ξ fluorescence stacks and (d-e) compares the vertical and horizontal line profiles along the dashed lines in (a-c). Both simulated and measured ξ show good correspondence with fluorescence in 3D, confirming that they are subject to blurring from the same incoherent PSF.

We demonstrate that with measurements of ξ at multiple depths and a knowledge of the PSF we can reconstruct the actual distribution ξ_0 within the sample. For this, we used a phantom containing two crossed capillaries, one above the other, connected by a plastic tube [Fig. 3(a)]. Diluted milk was pumped through both capillaries at a rate of 2 μL/min. 20 sequential frames were used to extract ξ in all six planes, shown in Fig. 3(f). The two capillaries were in focus in two different planes but blurred in all other planes. To correct for out-of-focus blur, we applied Richardson-Lucy (RL) deconvolution [20, 21] with a theoretically calculated PSF. The deconvolved result ξ_0 is shown in Fig. 3(g). The axial position of the two capillaries is well distinguished in the color-coded EDOF image of ξ_0 in Fig. 3(c).

Figure 3(d) shows a map of the reconstructed inverse correlation time τ_c^{-1} (ICT) at depth $-2\Delta z$, where one capillary was in focus and the other was not. We observe that the ICTs of both capillaries incorrectly appear different because of blur-induced error in one of the capillaries. For comparison, we show a synthesized all-in-focus ICT map in Fig. 3(e). Specifically, after reconstructing six ICT maps in all six planes using Eq.(12), we synthesized an all-in-focus ICT map by determining the plane index where ξ_0 was maximized and selecting the corresponding ICT value to form a 2D map. In effect, the indices of maximum ξ_0 form a depth map that selects only in-focus signal. In addition, the all-in-focus ξ_0 image in Fig. 3(c) was binarized to generate a mask, which was then applied to the ICT map to help suppress extraneous noise. It can be seen that the resulting all-in-focus ICT map now correctly reveals the same correlation time τ_c for both connected capillaries, even though these were located at different depths.

Finally, we demonstrate in-vivo mouse brain imaging with multifocus LSCI. We used an adult male wild-type mouse (C57BL/6J, #0000664, Jackson Laboratory, Bar Harbor, Maine). All procedures were approved by the Boston University Institutional Animal Care and Use Committee (IACUC). Following a craniotomy, a cranial window was implanted and a headplate was attached as described in [22, 23]. During imaging, the mouse was anesthetized and head-fixed to ensure minimal skull movement. The exposure was T = 5 ms, and K_t was calculated from 20 sequential frames averaged 5 times.

From the spatial and temporal contrasts K_s^2 and K_t^2, the dynamic fraction ξ at the six different depths was extracted and deconvolved to correct for blurring. Figure 4(a) shows the resulting all-in-focus EDOF image of ξ_0. A square region from a single depth before and after deconvolution is compared in Fig. 4(b–c). Deconvolution suppresses out-of-focus blur around the vessels and increases lateral resolution, as shown in the line profile in Fig. 4(d). The overall signal to background ratio (SBR), measured as the ratio of the vessel signal and local background from surrounding pixels, increases more than 3 times [Fig. 4(e)].

Figure 4(f) shows an EDOF ICT map of the mouse cortex processed in the same manner as described above for the phantom sample. We select two regions of interests (white boxed) and compare their correlation times calculated at in-focus (0) and out-of-focus (Δz) depths. The results are shown in Fig. 4(g), where the pulsations apparent in Fig. 4(g) arise from the mouse heart-beat rate of about 7 Hz. We observe that in both regions the ICT is smaller when the sample is out of focus than when it is in focus, even though ICT was calculated the same way in both cases by fitting to Eq. 12. The underestimation of ICT is caused by the errors in ξ arising from misfocus, which ultimately would cause errors when attempting to perform quantitative comparisons of flow speeds in different vessels or before and after a stimulus [24], prescribing the use of an all-in-focus ICT map instead.

In summary, we have shown that defocus can lead to errors in the determination of the dynamic fraction ξ, which, in turn can lead to errors in the determination of ICT when performing LSCI. These errors can be mitigated with the use of multifocus imaging, which can readily be achieved with a z-splitter and a single camera. In particular, multifocus imaging enables the retrieval by deconvolution of a depth-resolved ξ_0 map with improved SBR. Deconvolution of ξ as opposed to, for example, $1/K^2$ [13] is supported by theory and has the advantage producing structural maps independent of flow speed. The same is true when comparing with autofocus algorithms which seek to maximize measured flow speed and are thus also explicitly dependent on flow [14]. By evaluating best focus based on a determination of ξ_0 alone, free of the influence of flow speed, we render our measurements less susceptible to imaging-induced error, helping improve the ability of LSCI to be quantitative.

Funding.

National Institutes of Health R01NS116139, R21GM128020.

Data Availability Statement.

The data that support the findings of this study are available from the corresponding author upon reasonable request.

FULL REFERENCES

1. Vaz PG, Humeau-Heurtier A, Figueiras E, Correia C, and Cardoso J, “Laser speckle imaging to monitor microvascular blood flow: a review,” IEEE Rev. Biomed. Eng 9, 106–120 (2016). [PubMed: 26929060]
2. Fercher A and Briers JD, “Flow visualization by means of single-exposure speckle photography,” Opt. Commun 37, 326–330 (1981).

3. Cheng H, Luo Q, Zeng S, Chen S, Cen J, and Gong H, "Modified laser speckle imaging method with improved spatial resolution," J. Biomed. Opt 8, 559–564 (2003). [PubMed: 12880364]
4. Boas DA and Yodh AG, "Spatially varying dynamical properties of turbid media probed with diffusing temporal light correlation," J. Opt. Soc. Am. A 14, 192–215 (1997).
5. Lemieux P-A and Durian D, "Investigating non-gaussian scattering processes by using nth-order intensity correlation functions," J. Opt. Soc. Am. A 16, 1651–1664 (1999).
6. Parthasarathy AB, Tom WJ, Gopal A, Zhang X, and Dunn AK, "Robust flow measurement with multi-exposure speckle imaging," Opt. Express 16, 1975–1989 (2008). [PubMed: 18542277]
7. Parthasarathy AB, Kazmi SS, and Dunn AK, "Quantitative imaging of ischemic stroke through thinned skull in mice with multi exposure speckle imaging," Biomed. Opt. Express 1, 246–259 (2010). [PubMed: 21258462]
8. Wang Y, Wen D, Chen X, Huang Q, Chen M, Lu J, and Li P, "Improving the estimation of flow speed for laser speckle imaging with single exposure time," Opt. Lett 42, 57–60 (2017). [PubMed: 28059177]
9. Wang C, Cao Z, Jin X, Lin W, Zheng Y, Zeng B, and Xu M, "Robust quantitative single-exposure laser speckle imaging with true flow speckle contrast in the temporal and spatial domains," Biomed. Opt. Express 10, 4097–4114 (2019). [PubMed: 31452997]
10. Bandyopadhyay R, Gittings A, Suh S, Dixon P, and Durian DJ, "Speckle-visibility spectroscopy: A tool to study time-varying dynamics," Rev. Sci. Instruments 76, 093110 (2005).
11. Ramirez-San-Juan J, Ramos-Garcia R, Martinez-Niconoff G, and Choi B, "Simple correction factor for laser speckle imaging of flow dynamics," Opt. Lett 39, 678–681 (2014). [PubMed: 24487897]
12. Valdes CP, Varma HM, Kristoffersen AK, Dragojevic T, Culver JP, and Durduran T, "Speckle contrast optical spectroscopy, a non-invasive, diffuse optical method for measuring microvascular blood flow in tissue," Biomed. Opt. Express 5, 2769–2784 (2014). [PubMed: 25136500]
13. Sigal I, Gad R, Caravaca-Aguirre AM, Atchia Y, Conkey DB, Piestun R, and Levi O, "Laser speckle contrast imaging with extended depth of field for in-vivo tissue imaging," Biomed. Opt. Express 5, 123–135 (2014).
14. Ringuette D, Sigal I, Gad R, and Levi O, "Reducing misfocus-related motion artefacts in laser speckle contrast imaging," Biomed. Opt. Express 6, 266–276 (2015). [PubMed: 25657891]
15. Lv W, Wang Y, Chen X, Fu X, Lu J, and Li P, "Enhancing vascular visualization in laser speckle contrast imaging of blood flow using multi-focus image fusion," J. Biophotonics 12, e201800100 (2019). [PubMed: 29952071]
16. Xiao S, Gritton H, Tseng H.-a., Zemel D, Han X, and Mertz J, "High-contrast multifocus microscopy with a single camera and z-splitter prism," Optica 7, 1477–1486 (2020). [PubMed: 34532564]
17. Mertz J, Introduction to optical microscopy (Cambridge University Press, 2019).
18. Liu C, Kılıç K, Erdener SE, Boas DA, and Postnov DD, "Choosing a model for laser speckle contrast imaging," Biomed. Opt. Express 12, 3571–3583 (2021). [PubMed: 34221679]
19. Postnov DD, Tang J, Erdener SE, Kılıç K, and Boas DA, "Dynamic light scattering imaging," Sci. Adv 6, eabc4628 (2020).
20. Richardson WH, "Bayesian-based iterative method of image restoration," J. Opt. Soc. Am 62, 55–59 (1972).
21. Lucy LB, "An iterative technique for the rectification of observed distributions," The Astron. J 79, 745 (1974).
22. Cruz-Martín A, Crespo M, and Portera-Cailliau C, "Delayed stabilization of dendritic spines in fragile x mice," J. Neurosci 30, 7793–7803 (2010). [PubMed: 20534828]
23. Cruz-Martín A, El-Danaf RN, Osakada F, Sriram B, Dhande OS, Nguyen PL, Callaway EM, Ghosh A, and Huberman AD, "A dedicated circuit links direction-selective retinal ganglion cells to the primary visual cortex," Nature 507, 358–361 (2014). [PubMed: 24572358]
24. Dunn AK, Devor A, Dale AM, and Boas DA, "Spatial extent of oxygen metabolism and hemodynamic changes during functional activation of the rat somatosensory cortex," Neuroimage 27, 279–290 (2005). [PubMed: 15925522]

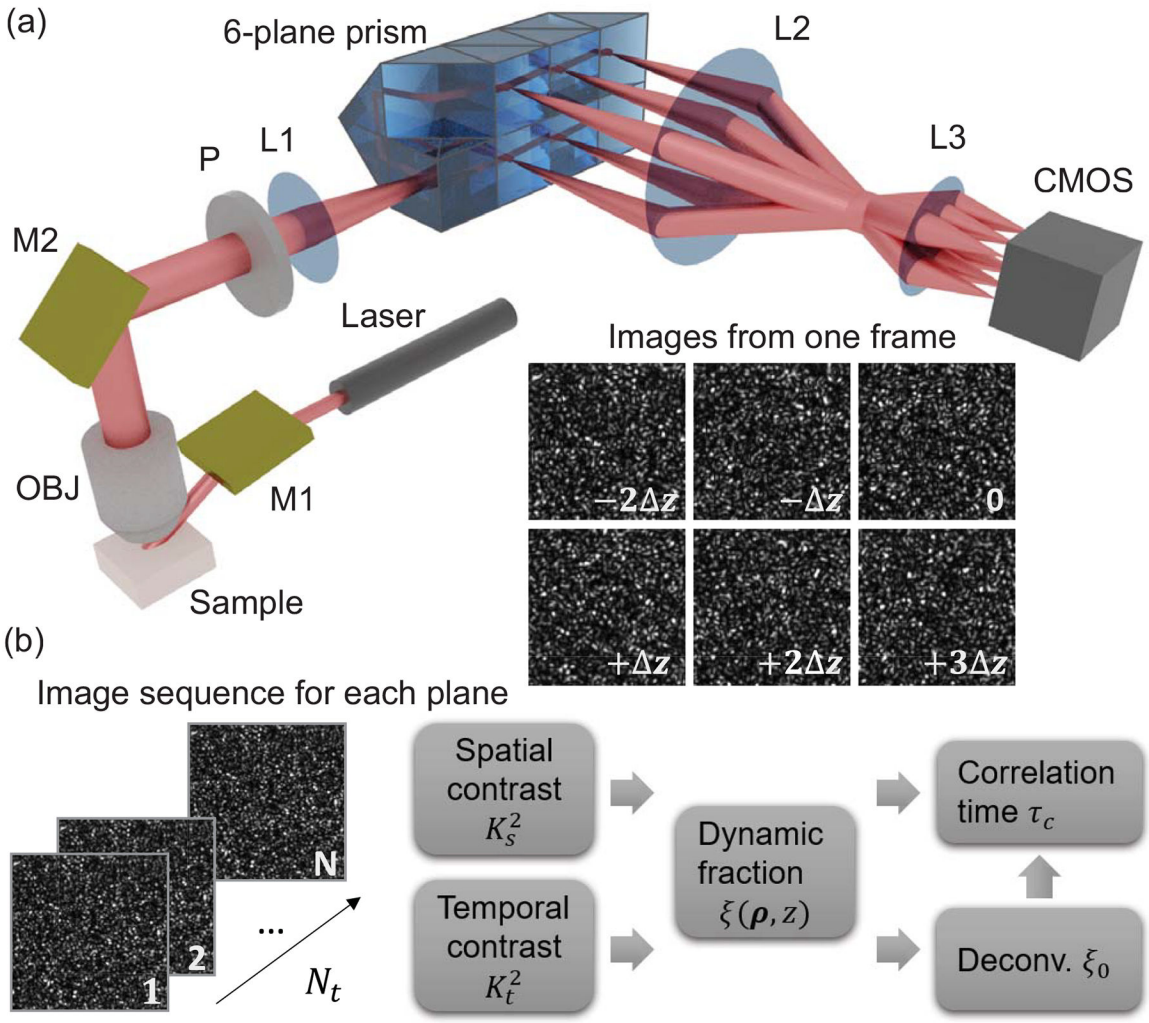

Fig. 1.

(a) Left: Schematic of setup. Right: 6-plane speckle images obtained in single camera frame. (b) Left: Example image sequence recorded in one plane. Right: Diagram of processing pipeline.

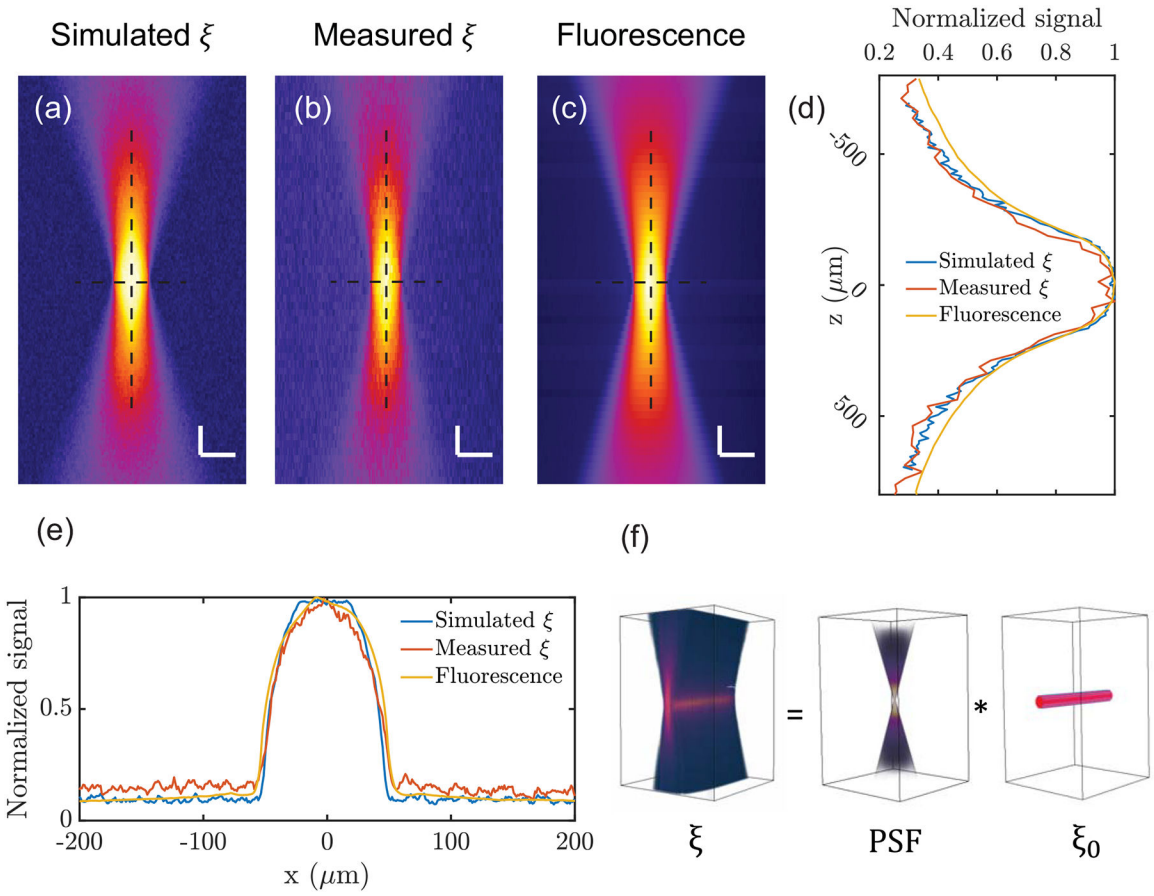

Fig. 2.

x-z cross section of a ξ stack obtained from simulated (a) and experimental (b) data. (c) *x-z* cross section of associated fluorescence image stack. (d-e) Line profiles along the vertical and horizontal dashed lines in (a)-(c). (f) Convolution model relating ξ and ξ_0. Scale bar in (a)-(c): 100 μm.

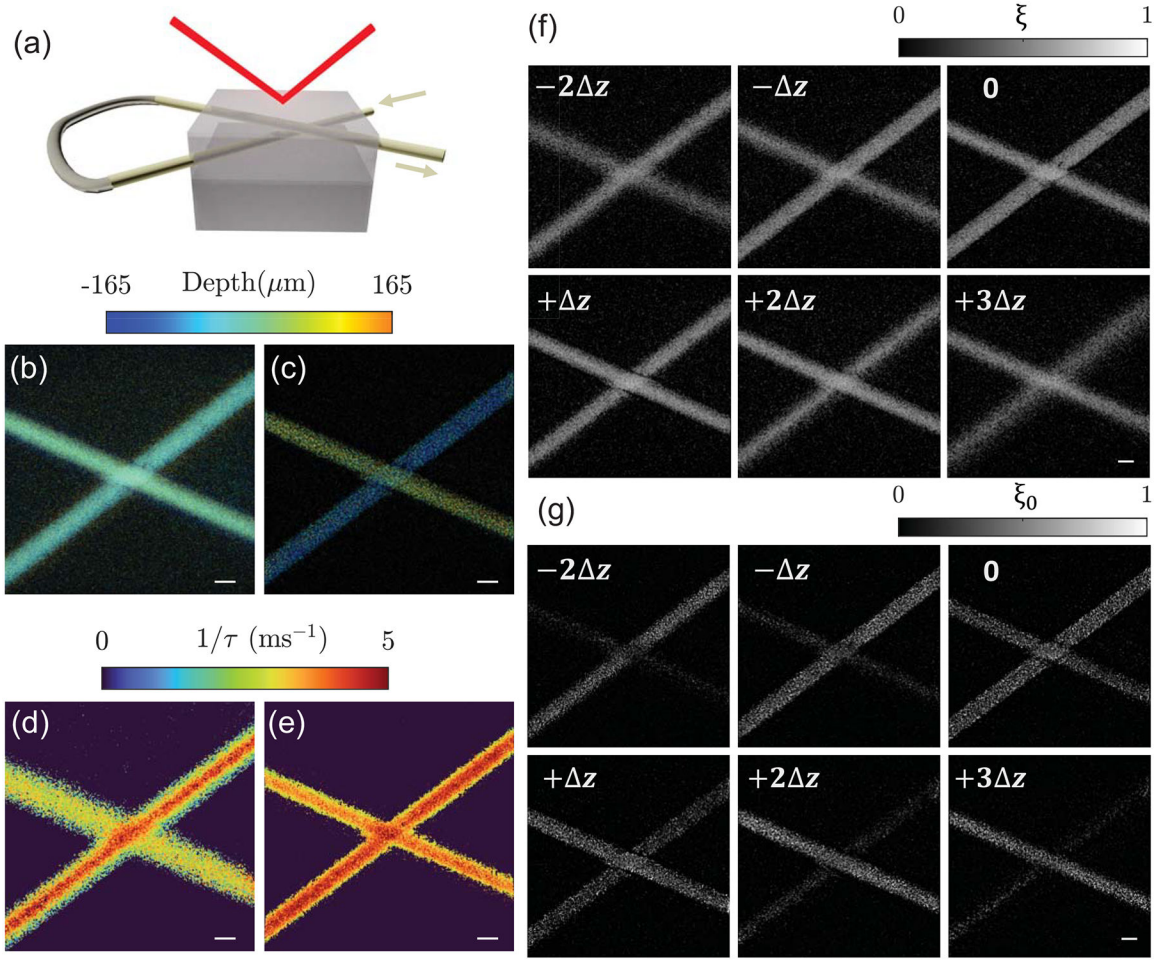

Fig. 3.

(a) Schematic of two capillaries embedded in a scattering medium. (b) EDOF projection of ξ. (c) All-in-focus EDOF image of ξ_0. (d) ICT map measured at depth $-2\Delta z$ with one capillary out of focus. (e) Synthetic all-in-focus ICT map of the capillaries. (f) Raw ξ map at six depths. (g) ξ_0 map at six depths. Scale bar in (b-g): 100 μm. Δz = 66 μm.

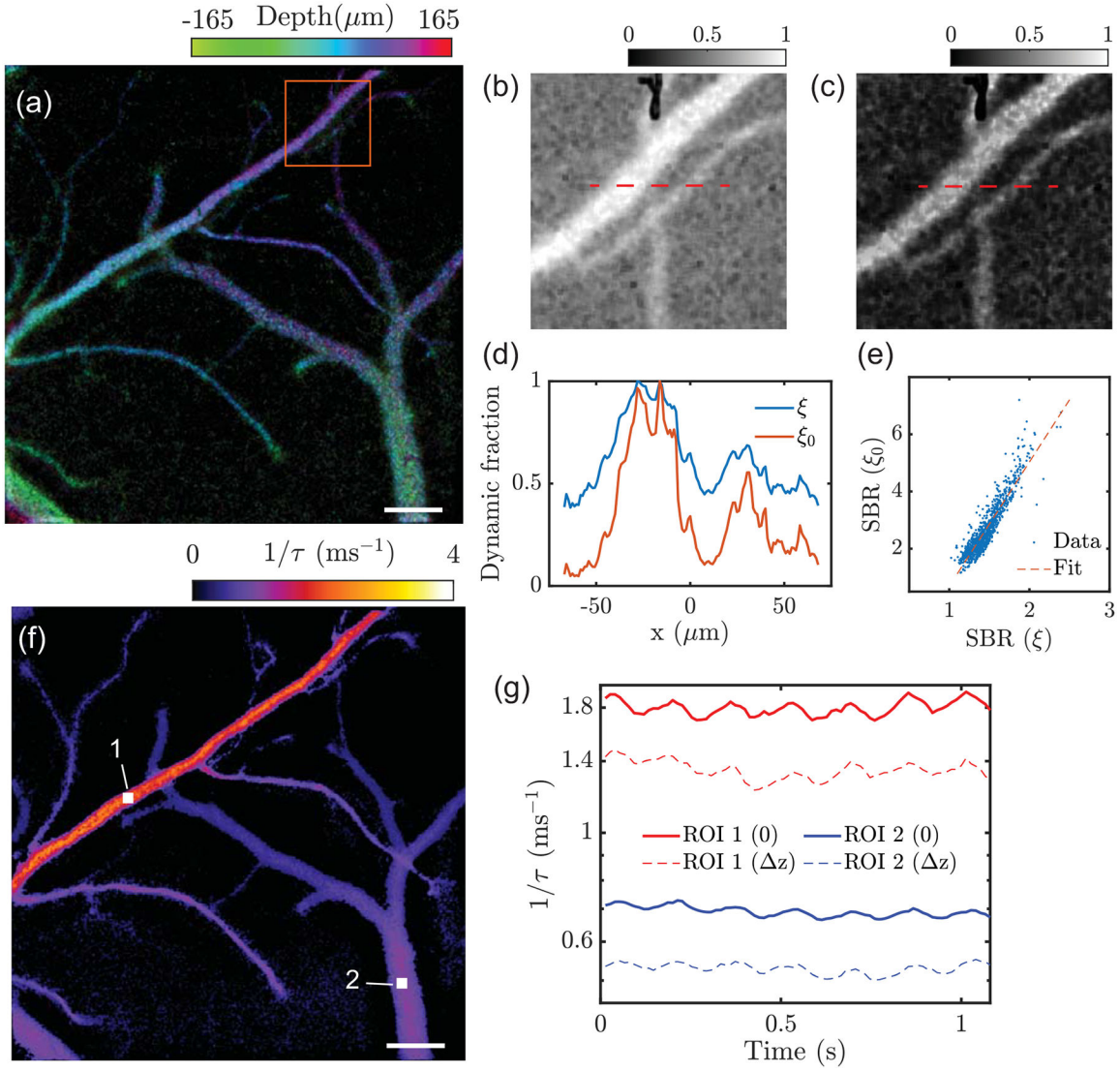

Fig. 4.

(a) All-in-focus EDOF image of ξ_0 in a mouse cortex. (b) Raw ξ image of the boxed region in (a). (c) ξ_0 in the boxed region after deconvolution. (d) Line profile of ξ before and after deconvolution along the dashed line in (b,c). (e) Signal-to-background ratio of ξ before and after deconvolution. (f) All-in-focus EDOF ICT map of the mouse cortex. (g) Time resolved ICT traces in ROI 1 and ROI 2 indicated by the solid boxes in (f). ICTs derived from in-focus (0) and out-of-focus (Δz) ROIs are compared. Scale bar in (a), (f): 100 μm. Background in these panels was masked based on a threshold in ξ_0 to highlight medium-sized blood vessels of interest.